5

Stability Boundary and Transparency for Haptic Rendering

Iñaki Díaz and Jorge Juan Gil
CEIT and TECNUN, University of Navarra
Spain

Thomas Hulin
Institute of Robotics and Mechatronics, German Aerospace Center (DLR)
Germany

1. Introduction

Over the past years haptic interfaces have been successfully integrated into a wide range of fields such as engineering (Borro et al., 2004) or surgery (Basdogan et al., 2004). Haptic devices allow users to interact with a certain environment, either remote or virtual, by the sense of touch. In these applications—unlike in conventional robotic systems—the user shares workspace with the device. Therefore, an unstable behaviour can damage the device, or even worse, harm the operator. Thus, stability must be guaranteed to ensure user safety and achieve high haptic performance. Unfortunately, preserving haptic stability usually implies reducing the range of dynamic impedances achievable by the system. Hence, rigid virtual objects cannot be perceived as stiff as real ones, and the overall haptic performance and transparency perception are considerably degraded.

Developing stable controllers able to exhibit a wide dynamic range of impedances is a persistent challenge in the field of haptics. This chapter describes main research carried out by the authors on stability issues for haptic rendering, as well as on the development of transparent haptic controllers.

In a haptic system, the stability boundary for haptic rendering depends on many factors, such as inherent interface dynamics, motor saturation, sensor resolution or time delay. Section 2 introduces the state-of-the-art on stability studies showing the influence of many of these phenomena. Beyond related work, Section 3 analyses the influence of viscous damping and delay on the stability boundary for haptic rendering. Although the shape of the stability boundaries found is quite complex, a linear condition which summarises the relation between virtual stiffness, viscous damping and delay is proposed.

Section 4 analyses the influence of the first vibration mode of the system on the stability boundary. The majority of haptic models used to analyse stability do not consider the existence of internal vibration modes. However, it will be shown that for certain interfaces vibration modes must be taken into account to correctly obtain the range of impedances achievable by the system.

Ensuring stability is of major concern in haptic interaction; however, preserving stability does not imply improving haptic transparency. A transparent haptic interface should be able to emulate any environment, from free-space to infinitely stiff obstacles without perceiving the dynamics of the haptic device. The stability boundary for haptic rendering is known to be independent of the mass of the device; yet, high inertia of haptic interfaces degrades both system usability and transparency. To cover this issue, Section 5 shows control algorithms that improve transparency on high-inertia haptic interfaces without compromising overall system stability. Finally, conclusions and future directions are drawn in Section 5.

2. Related Work

The authors of (Minsky et al., 1990) were the first to study the stability of haptic systems. They used the continuous model of a 1 DOF (degree-of-freedom) haptic device colliding against a virtual wall shown in Fig. 1. The interface has a mass m and a physical damping b. The user exerts a force F_u causing the displacement X_h of the device. An elastic model with stiffness K is used to compute the interaction force of the virtual environment.

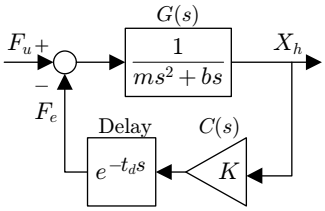

Fig. 1. Continuous haptic model.

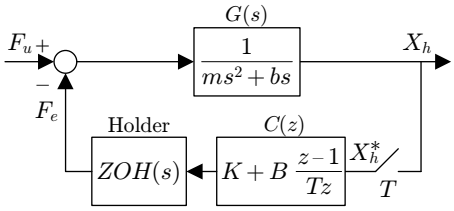

Fig. 2. Discrete haptic model.

In their study, system instabilities were attributed to the time delay introduced by the holder. To analyse its effect, but maintaining the continuous model, they included a time delay of one sampling period T to the actuation of the virtual environment. In this model, if the function of the delay is approximated by a second-order Taylor series expansion, it can be demonstrated that the system is stable if it satisfies the following condition:

$$b > KT \tag{1}$$

After this result, Minsky demonstrates experimentally that introducing in the model the user's mass m_h, damping b_h and stiffness k_h parameters, as well as a virtual damping B, the stability condition that must be guaranteed is:

$$B + b + b_h > \frac{(K + k_h)T}{2} \tag{2}$$

In this expression, the proportional factor $\frac{1}{2}$ is found from experimental results on the real system, but with no theoretical foundation. Later works (Brown & Colgate, 1994) show experimental results that obtain the stability boundary for haptic rendering as a function of many parameters of the device. Those results match the work carried out by Minsky.

From the control point of view, a haptic system is a sampled-data controlled mechatronic device. Unlike previous works, (Gil et al., 2004) analyse theoretically stability over a discrete haptic system (Fig. 2). $ZOH(s)$ represents the zero-order holder and the backwards difference is used to estimate velocity. The authors obtain the same stability condition (2) found by

previous works. Results of their work also show that this approximation is only valid for low values of virtual damping B. However, in most cases it is sufficient since common actuators used in haptic devices do not allow implementing large values of K and B.
The haptic models presented until now have not taken into account many parameters, such as user dynamics, friction, sensor quantization or time delays, that may have influence on stability. Regarding the user, (Gil et al., 2004), (Hulin, Preusche & Hirzinger, 2008) and (Diolaiti et al., 2006) show that the user only contributes positively to stability. Therefore, a haptic model without the user can be considered as the "worst-case scenario".
Fig. 3 shows the model of a haptic device colliding against a virtual wall with time delay t_d. This time delay can be the sum of several effects: computations, communications, etc. The model has also Coulomb friction c, and considers position sensor resolution q.

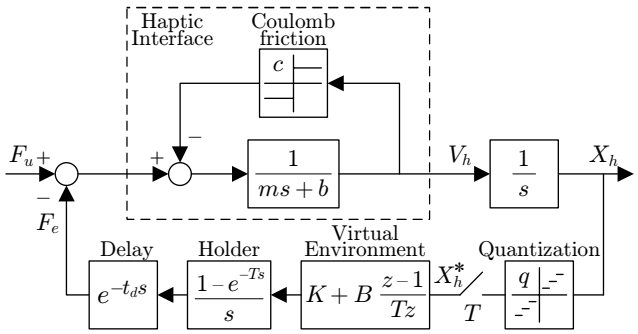

Fig. 3. Model of a haptic system with non-linear effects.

In (Diolaiti et al., 2006) and (Abbott & Okamura, 2005), it was found that Coulomb friction can dissipate the energy introduced by the quantization. Therefore, in some way both factors cancel each other and could be not considered for the stability analysis. Regarding the influence of the time delay, it will be covered in the following section.
Another way to guarantee the stability of the system is ensuring its passivity (Adams & Hannaford, 1999). The passivity condition for the system without time delay proposed by (Colgate & Schenkel, 1997) is

$$b > \frac{KT}{2} + B. \tag{3}$$

Notice that in (3) the virtual damping term does not contribute to obtain larger values of stiffness as in (2), but the opposite. Therefore, the passivity condition is considered a more restrictive condition than stability.
In later works, (Hannaford & Ryu, 2002) and (Ryu et al., 2005) have managed to adjust the passivity region using the "passivity controller". It consist of a variable virtual damping that dissipates the energy generated by the haptic interface. However, the model is still conservative compared to stability conditions.

3. Obtaining the Stability Boundary for Haptic Rendering

This section analyses the influence of viscous damping and delay on the stability boundary for haptic rendering. Assuming that Coulomb friction can dissipate the amount of energy introduced by quantization, and that the user only contributes positively to make the system

more stable, Fig. 4 shows a simplified haptic model that can be considered as the "worst-case scenario".

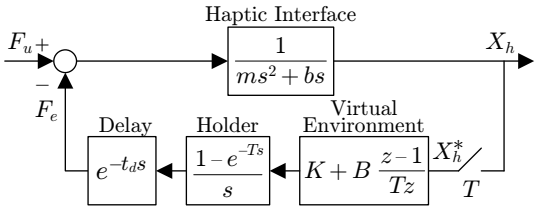

Fig. 4. Linear simplified model of a haptic system.

Following (Hulin et al., 2006), the dimensionless parameters that will be used in this section are shown in Table 1. Although some authors (Diolaiti et al., 2006) have used the virtual stiffness to normalise the parameters, here it will be used the mass (or the inertia for rotary joints), because this way the values of the device do not change with the contact force law.

Parameter	Variable	Dimensionless variable
Sampling period	T	-
Mass	m	-
Physical damping	b	$\delta = \frac{bT}{m}$
Virtual stiffness	K	$\alpha = \frac{KT^2}{m}$
Virtual damping	B	$\beta = \frac{BT}{m}$
Delay	t_d	$d = \frac{t_d}{T}$

Table 1. Dimensionless parameters.

Both real and dimensionless parameters can theoretically take any value ($m > 0$, $b > 0$, $T > 0$ and $t_d \geq 0$). However, typical sampling rates in haptics are quite fast ($\geq$ 1 kHz) and the relation between the physical damping and the mass cannot be supposed to be arbitrarily large. For example, some experimentally acquired values given in (Diolaiti et al., 2006) show that $\frac{b}{m} \ll 1\ \mathrm{s}^{-1}$ for all investigated haptic devices. Therefore, the dimensionless physical damping δ is quite small in haptic systems. In this study it will be supposed that $\delta < 10^{-3}$.
Classical control tools have been applied to the linear system in order to obtain the stability conditions. In (Gil et al., 2004), it was stated that, with no delay, $d = 0$, the stability condition of the linear system (using the dimensionless parameters of Table 1) is

$$\alpha < \delta(\delta+\beta)\frac{(1-\epsilon)(\beta\epsilon+\beta\delta\epsilon-\beta+\delta^2)}{(1-\epsilon-\delta\epsilon)(\beta\epsilon+\beta\delta-\beta+\delta^2)}, \tag{4}$$

where ϵ is a dimensionless number,

$$\epsilon = e^{-\frac{bT}{m}} = e^{-\delta}. \tag{5}$$

Stability condition (4) is consistent with (Gillespie & Cutkosky, 1996). Substituting ϵ by its Taylor approximation,

$$\epsilon = 1 - \delta + \frac{1}{2}\delta^2 - \frac{1}{6}\delta^3 + O(\delta^4), \tag{6}$$

makes it possible to linearise (4) around the origin and to obtain the following more compact stability condition:

$$\alpha < 2(\delta + \beta). \tag{7}$$

The fact that the dimensionless physical damping δ is a very small number enforces the validity of this approximation. Further experimental studies confirm the result that increasing both the physical viscous damping—i.e. electrically (Mehling et al., 2005), (Tognetti & Book, 2006) or magnetically (Gosline et al., 2006)—and the virtual damping (Colgate & Brown, 1994), (Janabi-Sharifi et al., 2000) allows for larger stable stiffness coefficients.
If the system contains a delay of one sampling period, $d = 1$, the stability condition that has been proposed in (Bonneton & Hayward, 1994) using the Padé approximation is

$$\alpha < \frac{2}{3}(\delta + \beta). \tag{8}$$

3.1 Stability Condition

In this section, a stability condition for the linear system including the effect of both delay and virtual damping is proposed. This stability condition may be seen as generalisation of previous conditions (7) and (8) for any delay, consistent with the study of the non-linear system (Diolaiti et al., 2006) but including the effect of the virtual damping β:

$$\alpha < \frac{2}{1 + 2d}(\delta + \beta). \tag{9}$$

Using the physical values of the parameters the proposed stability condition is

$$K < \frac{b + B}{\frac{T}{2} + t_d}, \tag{10}$$

and taking into account that the effect of the sampling and hold in the control loop can be approximated by a delay of half the sampling period $\frac{T}{2}$, the stability condition proposed (10) can be interpreted with the following statement:

$$\text{Critical stiffness} = \frac{\sum \text{Damping}}{\sum \text{Delay}}. \tag{11}$$

The critical stiffness of a haptic system is equal to the overall damping of the mentioned system divided by the total delay of the loop. Therefore, a double viscous damping in the system—physical plus virtual—will allow for a double stiffness; while a double delay in the haptic loop—no matter its nature—will half the maximum stable stiffness.
The validity of this formula will be checked by two different ways: 1) solving numerically the characteristic equation and performing a graphical approach, 2) with experimental results. The reader is addressed to (Gil, Sánchez, Hulin, Preusche & Hirzinger, 2009) for a complete theoretical analysis.

3.2 Graphical Analysis

The methodology followed in (Gil et al., 2004) can be used to receive the analytical stability condition from the characteristic equation of the system. In the Z-domain, this equation consists of a polynomial if the delay t_d is a multiple of the sampling period T (then d takes natural

values):

$$\begin{aligned}\delta^2(z-\epsilon)(z-1)z^{d+1} - (1-\epsilon-\delta)(\alpha+\beta)z^2 \\ + \left[(1-\epsilon-\delta\epsilon)(\alpha+\beta) + (1-\epsilon-\delta)\beta\right] z \\ -(1-\epsilon-\delta\epsilon)\beta = 0.\end{aligned} \tag{12}$$

The validity of (9) is checked using the graphs of the stability boundaries. Two different ways have been used to obtain and depict the critical stiffness of the linear system with delay. The first one follows (Gil et al., 2004) and directly obtains the critical stiffness for different values of the virtual damping evaluating

$$\alpha < \mathrm{Gm}\left[\frac{1}{\frac{z^d(z-1)(z-\epsilon)\delta^2}{(\epsilon-1+\delta)z+1-\epsilon-\delta\epsilon} + \beta\frac{z-1}{z}}\right], \tag{13}$$

where Gm[.] means gain margin of the Z-transfer function. The second method, used in (Hulin et al., 2006) and (Salcudean & Vlaar, 1997), numerically solves the poles of the characteristic equation (12) and finds the stiffness coefficients which place all the poles just within the unit circle. Although both methods obtain the same results, the gain margin can be computed easily in Matlab® if the delay is a multiple of the sampling period T, while the other method allows for introducing fractional numbers for the delay. Fig. 5 shows the stability boundaries for different delays d, setting $\delta < 10^{-3}$.

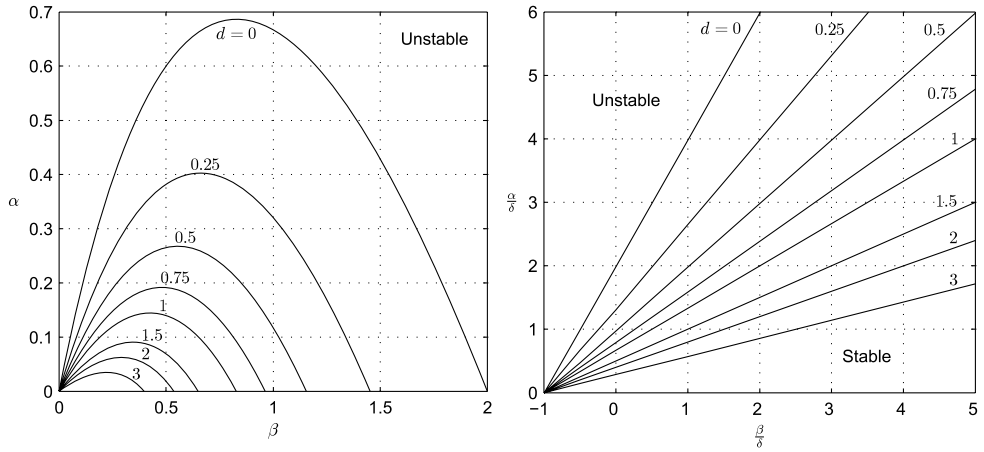

Fig. 5. Stability boundaries for small dimensionless physical damping ($\delta < 10^{-3}$) and delays $d = [0, 0.25, 0.5, 0.75, 1, 1.5, 2, 3]$ (left) and zoom near the point of origin (right).

The shown boundaries in Fig. 5 (right) fit perfectly the linearised stability condition (9). The initial slope of the stability boundaries becomes smaller with the delay. Therefore, the critical stiffness without virtual damping $\beta = 0$ decreases also with the delay. This means that, using the physical parameters, the critical stiffness depends on both the physical damping and the delay.

3.3 Experimental Results

Two different haptic interfaces have been used to perform experiments: the DLR Light-Weight Robot III (Hirzinger et al., 2002) and the LHIfAM (Savall et al., 2004). A bilateral virtual wall consisting of a virtual spring and damper was implemented using one joint of each interface. Limit-stable parameter values were obtained when sustained oscillations were observed increasing the stiffness. No user was involved in the experiments.

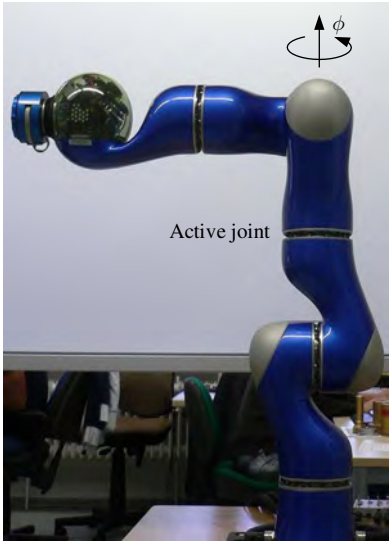

Fig. 6. Third generation of the DLR Light-Weight Robot arm.

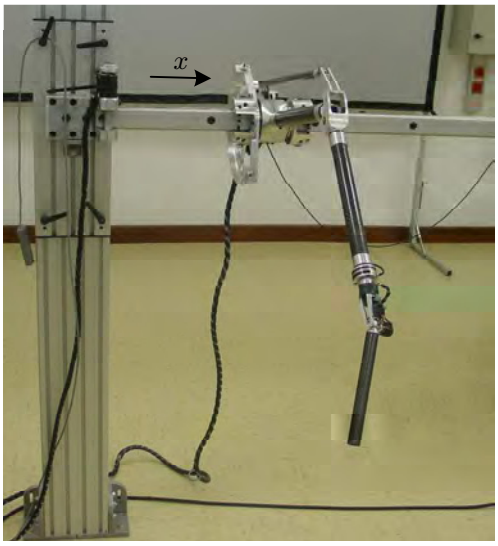

Fig. 7. LHIfAM haptic interface.

3.3.1 DLR Light-Weight Robot

The DLR Light-Weight Robot III (Fig. 6) is a 7 DOF robot arm with carbon fiber grid structure links. Though it weighs only 14 kg, it is able to handle payloads of 14 kg throughout the whole dynamic range. The electronics, including the power converters, is integrated into the robot arm. Every joint has an internal controller which compensates gravity and Coulomb friction. Since high-resolution position sensors are used to measure link orientation (quantization $q \approx$ 20"), non-linear effects can be neglected.

The virtual wall was implemented in the third axis of the robot, indicated by the rotating angle ϕ in Fig. 6. The environment was implemented using a computer connected to the robot via Ethernet. The sampling rate was 1 kHz and the overall loop contained a delay of 5 ms. Fig. 8 shows the experimental results, introducing several fixed values for the virtual damping. A set of experiments was performed with only the system delay of 5 ms, while additional delays were artificially introduced into the loop to obtain an overall delay of 6 and 10 ms. The theoretical behaviour is depicted with dashed lines. The experimental stability boundaries fit the linear condition remarkably well.

A significantly long delay was also introduced into the system in order to obtain a curved stability boundary. Fig. 9 shows the experimental stability boundary for an overall delay of 55 ms. The beginning of the stability boundary for a delay of 10 ms is also shown in the same

figure. The theoretical stability curve has been computed using the device's inertia in the configuration selected for the experiments: 0.8 kg·m^2.

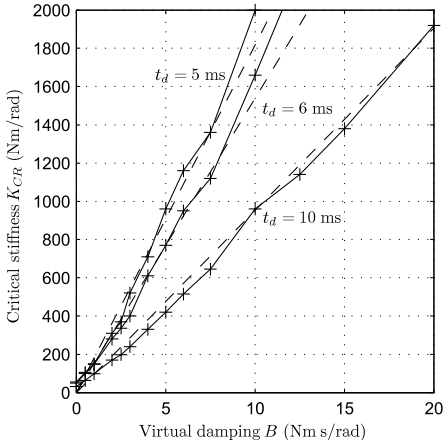

Fig. 8. Experimental stability boundaries for a delay t_d of 5, 6 and 10 ms (pluses and solid) and theoretical boundaries (dashed).

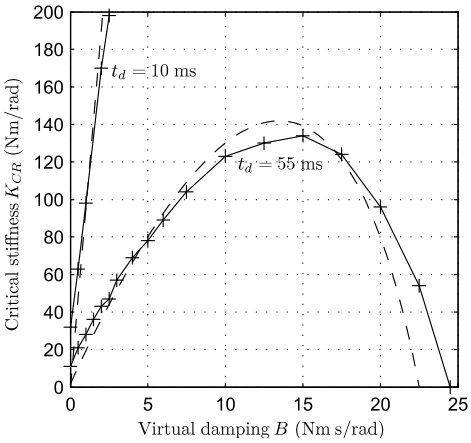

Fig. 9. Experimental stability boundaries for a delay t_d of 10 and 55 ms (pluses and solid) and theoretical boundaries (dashed).

3.3.2 LHIfAM

The LHIfAM (Fig. 7) is a haptic interface with a large workspace developed at CEIT. The mechanism consists of a counterbalanced parallelogram moving on a linear guide 1.5 m in length. The virtual wall was implemented in the direction of the translational movement of the guide (x axis in Fig. 7). In this direction, both the inertia of the device and the sensor resolution are quite high: 5.4 kg and quantization $q \approx 3.14$ μm, respectively. The Coulomb friction is compensated by the controller.

The controller can acquire the information from the sensor, compute the force of the virtual wall and command the motor within the same sampling period, that is, theoretically without delay in the loop. Therefore, significant stiffness coefficients can be implemented with stable behaviour. However, the motor is saturated with few millimeters of penetration in the virtual wall. In order not to saturate the actuator in the overall critical oscillation, artificial delays of 3, 6 and 12 ms have been introduced into the control loop.

Fig. 10 shows the experimental stability boundaries. It can be seen that experimental results match the stability condition proposed in (10). The theoretical stability boundaries have been computed using a physical damping of 4.6 Ns/m. Although the physical damping is quite high, since the sampling period was 1 ms, the dimensionless damping of the LHIfAM in the direction of x was $\delta = 0.85 \times 10^{-3}$ and therefore still within the $\delta < 10^{-3}$ range.

3.4 Valid Range of the Linear Condition

The shape of the stability boundary can be divided into two different parts. The first one follows the linear condition (10) for relatively small values of virtual damping (Fig. 8). The second one is a curve (Fig. 9) which can be obtained graphically or experimentally.

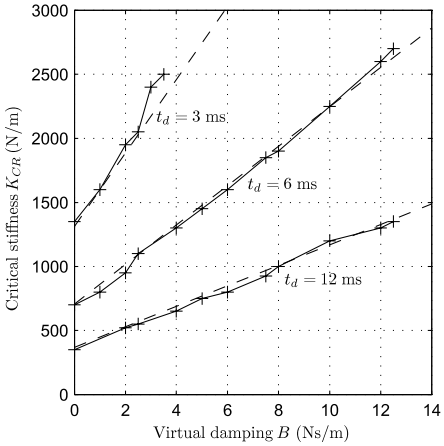

Fig. 10. Experimental stability boundaries for the LHIfAM and a delay t_d of 3, 6 and 12 ms (pluses and solid) and theoretical stability boundaries for a physical damping b of 4.6 Ns/m (dashed) and same delays.

Regarding the delay, several factors, such as computation of the collision detection algorithms for complex virtual environments, digital to analog conversion, and amplifier dynamics, introduce a certain delay in the haptic system that is usually equal to or less than one sampling period. Therefore the linear condition is appropriate for haptic devices. In other kinds of systems, which usually involve longer delays, the linear stability condition should no be used. For example, it is quite common to suppose a delay equal to hundreds of milliseconds in teleoperated systems.

4. Beyond Rigid Haptic Models: Influence of Internal Vibration Modes on Stability

The mathematical model used to analyse stability in previous section does not take into account the existence of internal vibration modes. This section presents a theoretical approach that studies the influence of internal vibration modes on the stability of haptic rendering (Díaz & Gil, 2008). In particular, it addresses the influence of the first resonant mode of cable transmission used in haptic devices. This type of mechanical transmission is widely used in haptic devices because it offers a number of advantages such as low friction, no backlash and low weight (Townsend, 1988).

4.1 Model Description

Fig. 11(a) illustrates the simplified model of a haptic device used in previous section to analyse the stability of haptic systems. It has a mass m and a viscous damping b, and the model assumes that the mechanical device is perfectly rigid. Although the force exerted by the motor F_r and the net force exerted by the user F_u are introduced in different places, a single transfer function is defined for this model, which is

$$G(s) = \frac{X}{F_r + F_u} = \frac{1}{ms^2 + bs}. \tag{14}$$

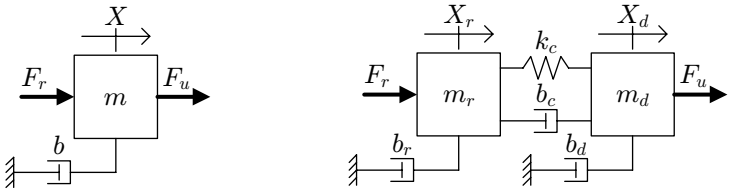

Fig. 11. Mechanical schematic of a perfectly rigid haptic device (a), and a haptic device with a single vibration mode (b).

Fig. 11(b) shows a haptic system with a single vibration mode. In this model, the device is divided into two masses connected by a link: mass m_r, pushed by the force of the motor, and mass m_d, pushed by the user. The dynamic properties of the link are characterised by a spring and a damper (k_c and b_c). This model is a two-input/two-output system, and the relationship between output positions and input forces is

$$\mathbf{x} = \begin{bmatrix} X_d \\ X_r \end{bmatrix} = \begin{bmatrix} G_d(s) & G_c(s) \\ G_c(s) & G_r(s) \end{bmatrix} \begin{bmatrix} F_u \\ F_r \end{bmatrix} = \frac{1}{p(s)} \begin{bmatrix} p_r(s) & k_c + b_c s \\ k_c + b_c s & p_d(s) \end{bmatrix} \begin{bmatrix} F_u \\ F_r \end{bmatrix} = \mathbf{G}\mathbf{f}, \tag{15}$$

where,

$$p_r(s) = m_r s^2 + (b_r + b_c)s + k_c, \tag{16}$$

$$p_d(s) = m_d s^2 + (b_d + b_c)s + k_c, \tag{17}$$

$$p(s) = p_r(s)p_d(s) - (k_c + b_c s)^2. \tag{18}$$

Introducing an impedance interaction with the virtual environment, the device can be analysed as a single-input/single-output system, as illustrated in Fig. 12. $C(z)$ is the force model of the virtual contact (which usually includes a spring and a damper), $H(s)$ is the zero-order-holder, T is the sampling period, and t_d represents the delay in the loop. The sampled position of the motor is given by

$$X_r^* = \frac{Z[G_c(s)F_h(s)]}{1 + C(z)Z[H(s)G_r(s)e^{-t_d s}]}. \tag{19}$$

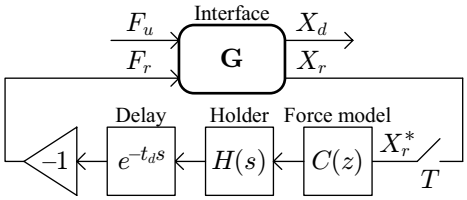

Fig. 12. Haptic system with impedance interaction.

If the force model only has a virtual spring with stiffness K, stability of the system depends on the following characteristic equation:

$$1 + KZ[H(s)G_r(s)e^{-t_d s}] = 0, \tag{20}$$

and the critical stiffness is

$$K_{CR} = \mathrm{Gm}\{Z[H(s)G_r(s)e^{-t_d s}]\}, \tag{21}$$

where Gm{.} means gain margin of the transfer function within brackets. From (21), it follows that $G_r(s)$ is the relevant transfer function for the stability of the system.

4.2 Model Parameters Identification

The physical parameters for $G_r(s)$ have been experimentally identified for two haptic interfaces, PHANToM 1.0 and LHIfAM. Since these interfaces are significantly different in terms of workspace and overall physical properties, the influence of the vibration modes may differ from one to another. Both devices are controlled by a dSPACE DS1104 board that reads encoder information, processes the control loop and outputs torque commands to the motor at 1 kHz.

A system identification method based on frequency response has been used to determine $G_r(s)$. This strategy has already been successfully used to develop a model of a cable transmission (Kuchenbecker & Niemeyer, 2005). The method yields an empirical transfer function estimate (ETFE), or experimental Bode plot (Ljung, 1999), by taking the ratio of the discrete Fourier transform (DFT) of the system's output response signal to the DFT of the input signal applied. A white noise signal is commonly used as input signal (Weir et al., 2008). Model parameters are identified by fitting the ETFE to the theoretical transfer function with six independent variables by performing an automatic iterative curve fitting using least-squares method.

The first rotating axis of a PHANToM 1.0 haptic interface has been used for the experiments (angle ϕ in Fig. 13). Only the motor that actuates this axis is active. A white noise torque signal is applied and the output rotation is measured. The experiment is performed without any user grasping the handle of the device.

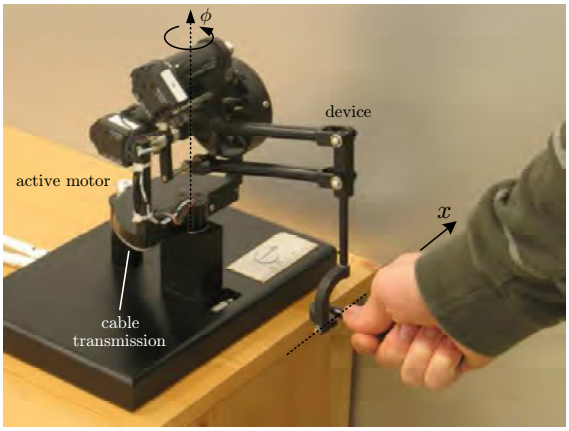

Fig. 13. PHANToM 1.0 haptic interface.

The frequency response of the system is presented in Fig. 14. It can be seen that the first vibration mode of the interface takes place at 62.5 Hz, which may correspond to the one detected in (Çavuşoğlu et al., 2002) at 60 Hz. The parameters obtained for $G_r(s)$ are presented in Table 2. These parameters have been identified with respect to the ϕ-axis.

Parameter	Variable	PHANToM	LHIfAM
Device mass	m	1.05 gm^2	5.4 kg
Device damping	b	0.0085 Nms/rad	3.5 Ns/m
Motor mass	m_r	0.895 gm^2	0.3 kg
Motor damping	b_r	0.0085 Nms/rad	0.1 Ns/m
Cable damping	b_c	0.0057 Nms/rad	15 Ns/m
Cable stiffness	k_c	18.13 Nm/rad	79.5 kN/m
Body mass	m_d	0.155 gm^2	5.10 kg
Body damping	b_d	0 Nms/rad	3.4 Ns/m

Table 2. Physical parameters of the PHANToM and the LHIfAM.

The equivalent translational parameters at the tip of the handle[1] (along the x-axis in Fig. 13) can be calculated by dividing the rotational parameters by $(12\text{ cm})^2$. The linear inertia results as $m = 72.92$ g, which is consistent with the manufacturer specifications: $m < 75$ g; and the linear damping as $b = 0.59$ Ns/m.

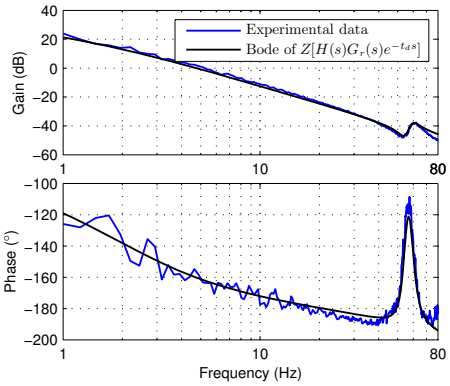

Fig. 14. Experimental (blue line) and theoretical (black line) Bode diagrams for the PHANToM.

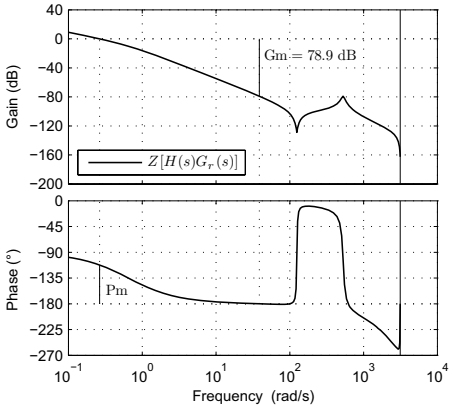

Fig. 15. Bode diagram and margins of $Z[H(s)G_r(s)]$ calculated for the LHIfAM.

Regarding the LHIfAM haptic interface, its translational movement along the guide has been used as a second testbed (Fig. 7). The cable transmission is driven by a commercial Maxon RE40 DC motor. Table 2 summarises the physical parameters obtained, and Fig. 15 shows the shape of $G_r(s)$ and the gain margin of the system.

4.3 Influence of the Vibration Mode

With the physical parameters obtained for both devices, $G_r(s)$ is known and the critical stiffness can be found by evaluating (21). If we compare those results with the linear condition (10) obtained in Section 3, the influence of the vibration mode on the critical stiffness, if any, can be found. Table 3 shows these theoretical gain margins for both devices.

[1] Placing the tip of the handle at the middle of the workspace is approximately at 12 cm from the joint axis.

Device	Model	Gm (dB)
PHANToM	Rigid	24.6
	Non rigid	22.41
LHIfAM	Rigid	76.9
	Non rigid	78.9

Table 3. Gain margins of PHANToM and LHIfAM.

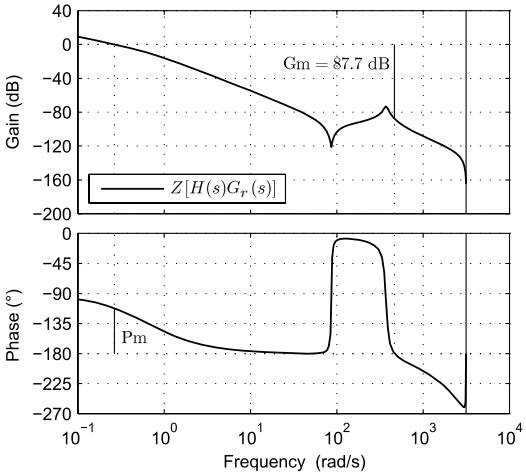

Fig. 16. Bode diagram and margins of $Z[H(s)G_r(s)]$ calculated for the LHIfAM after reducing cable pretension.

Gain margins obtained with the rigid haptic model are very similar to those obtained with a haptic model that takes into account the first vibration mode of the device. Therefore, it seems that the vibration mode does not affect stability. However, analysing Fig. 15, it can be seen that for the LHIfAM the resonant peak of the vibration mode could easily have imposed the stability margin. Therefore, further studies have been carried out on the LHIfAM to analyse the possible influence of the vibration mode. For that purpose, the initial pretension of the LHIfAM's cable transmission has been decreased. This affects directly the cable's dynamic parameters, thus the vibration mode. New parameters are: $k_c = 38$ kN/m and $b_c = 11$ Ns/m. Fig. 16 shows the Bode diagram of $Z[H(s)G_r(s)]$ for the new cable transmission setup. In this case, the first resonant mode of the cable does impose the gain margin of the system. Notice that the new gain margin is larger than the one of the original system, but placed at a higher frequency. Although it may not seem evident in Fig. 16, there is only one phase crossover frequency at 411.23 rad/s in the Bode diagram.
A possible criterion to estimate whether the resonant peak influences on the critical stiffness is to measure the distance Q from the resonant peak to 0 dB. This distance is approximately

$$Q \approx m_r z_n \omega_n, \tag{22}$$

where,

$$z_n = \frac{b_r + b_c}{m_r} + \frac{b_d + b_c}{m_d} - \frac{b_r + b_d}{m_r + m_d}, \tag{23}$$

$$w_n = \sqrt{\frac{k_c(m_r + m_d)}{m_d m_r}}. \tag{24}$$

Distance Q should be compared with the critical stiffness obtained using the criterion presented in (10), which gives a gain margin similar to the one shown in Fig. 15. If Q is similar or larger than that value, then the vibration mode should be taken into account in the stability analysis. Using the parameters of the LHIfAM, Q is approximately 78.16 dB (with original cable setup).

4.4 Experimental Results

Theoretical results of the influence of the vibration mode on the gain margin of the LHIfAM have been validated experimentally. Experiments have been performed after reducing cable pretension, therefore the gain margin obtained should be placed on the resonant peak of the vibration mode.

An interesting approach is to experimentally seek out—by tuning a controllable parameter in the same system—several critical stiffness values K_{CR}: some that are influenced by the resonant frequency and others that are not. This can be achieved by introducing an elastic force model with different time delays t_d:

$$C(z) = Kz^{-\frac{t_d}{T}}. \tag{25}$$

This way, the characteristic equation becomes

$$1 + Kz^{-\frac{t_d}{T}} Z[H(s)G_r(s)] = 0, \tag{26}$$

and the critical stiffness is

$$K_{CR} = \mathrm{Gm}\{z^{-\frac{t_d}{T}} Z[H(s)G_r(s)]\} = \mathrm{Gm}\{Z[H(s)G_r(s)e^{-t_d s}]\}. \tag{27}$$

Without any delay in the system, the gain margin should be imposed by the resonant peak of the vibration mode. Introducing certain time delay within the loop the gain margin should move to the linear region of the Bode where the slope is -40 dB/decade (as it is schematically shown in Fig. 17).

The critical virtual stiffness of the device has been calculated by means of the relay experiment described in (Barbé et al., 2006; Gil et al., 2004; Åström & Hägglund, 1995), with and without time delay. In this experiment a relay feedback—an on-off controller—makes the system oscillate around a reference position. In steady state, the input force is a square wave, the output position is similar to a sinusoidal wave, both in counterphase. These two signals in opposite phase are shown in Fig. 18.

It can be demonstrated (Åström & Hägglund, 1995) that the ultimate frequency is the oscillation frequency of both signals, and the critical gain is the quotient of the amplitudes of the first harmonic of the square wave and the output position. Since we are relating force exerted on the interface and position, this critical gain is precisely the maximum achievable virtual stiffness for stability.

Nine trials with varying delays in the input force (from 0 to 8 ms) were performed. Each one of these trials was repeated four times in order to have consistent data for further analysis. In each experiment, input-output data values were measured for more than 15 seconds (in steady state). Oscillation frequencies were found by determining the maximum peak of the average power spectral density of both signals. Gain margins were obtained by evaluating

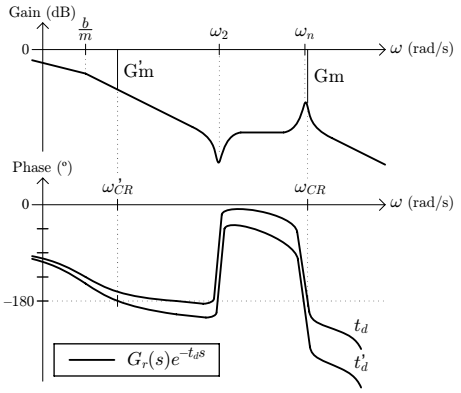

Fig. 17. Scheme of the Bode diagram of $G_r(s)e^{-t_d s}$ for two different time delays ($t_d < t'_d$).

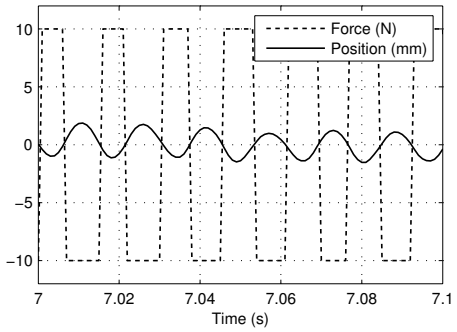

Fig. 18. Force input and position output of a relay experiment for time delay $t_d = 0$.

t_d (ms)	ω_{CR} (Hz)	Gm (dB)	t_d (ms)	ω_{CR} (Hz)	Gm (dB)	t_d (ms)	ω_{CR} (Hz)	Gm (dB)
0	64.9414	80.3149	3	4.3945	73.5975	6	3.1738	66.8281
0	64.4531	79.9414	3	4.3945	73.8443	6	3.1738	66.7219
1	60.0586	76.2336	4	4.3945	73.5919	7	2.6855	64.1268
1	59.0820	75.3235	4	4.3945	73.6444	7	2.8076	64.6013
2	4.8828	76.1063	5	4.5166	73.9604	8	2.3193	61.3209
2	4.8828	76.4240	5	4.3945	73.3171	8	2.3193	61.4755

Table 4. Critical oscillations of the LHIfAM.

the estimated empirical transfer function at that frequency. Table 4 presents these oscillation frequencies and gain margins.

Fig. 19 shows that results of Table 4 and the Bode diagram of $Z[H(s)G_r(s)]$ calculated for the LHIfAM match properly. Notice that the resonant peak of the vibration mode determines the stability of the system only for short delays.

Critical gain margins shown in Table 4 for the undelayed system should be similar to the gain margin obtained theoretically in Fig. 16. However, they differ more than 7 dB. A possible reason could be that most practical systems experience some amplifier and computational delay in addition to the effective delay of the zero-order holder (Diolaiti et al., 2006). This inherit delay has been estimated using the Bode diagram of Fig. 16, and is approximately 250 μs.

To sum up, the analysis carried out on this section shows that the first resonant mode of the haptic device can affect the stability boundary for haptic interfaces in certain cases. Therefore, the designer of haptic controllers should be aware of this phenomena to correctly display the maximum stiffness without compromising system stability.

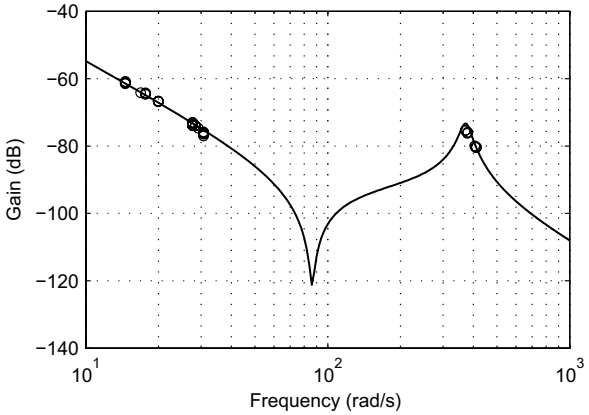

Fig. 19. Experimental gain margins obtained for several time delays by the relay experiment (circles), and the Bode diagram of $Z[H(s)G_r(s)]$ calculated for the LHIfAM (line).

5. Improving Transparency for Haptic Rendering

The need to decrease the inertia of an impedance haptic interface arises when a mechanism with large workspace is used. This occurs with the LHIfAM haptic device, which was designed to perform accessibility and maintenance analyses by using virtual reality techniques (Borro et al., 2004). One important objective of the mechanical design was to incorporate a large workspace while maintaining low inertia—one of the most important goals needed to achieve the required transparency in haptic systems. The first condition was met by using a linear guide (Savall et al., 2008). However, the main challenge in obtaining a large workspace using a translational joints is the high level of inertia sensed by the user. If no additional actions are taken, the operator tires quickly; therefore a strategy to decrease this inertia is needed.

A simple strategy used to decrease the perceived inertia is to measure the force exerted by the operator and exert an additional force in the same direction of the user. This type of feed-forward force loop, described in (Carignan & Cleary, 2000) and (Frisoli et al., 2004), has been successfully used in (Bernstein et al., 2005) to reduce the friction of the Haptic Interface at The University of Colorado. In (Ueberle & Buss, 2002), this strategy was used to compensate gravity and reduce the friction of the prototype of ViSHaRD6. It has also been used in (Hashtrudi-Zaad & Salcudean, 1999) for a teleoperation system. In (Hulin, Sagardia, Artigas, Schätzle, Kremer & Preusche, 2008), different feed-forward gains for the translational and rotational DOF are applied on the DLR Light-Weight Robot as haptic device.

To decrease the inertia of the haptic interface, the force exerted by the operator is measured and amplified to help in the movement of the device (Fig. 20). The operator's force F_u is measured and amplified K_f times. Notice that F_h is the real force that the operator exerts, but owing to the dynamics of operator's arm, $Z_h(s)$, a reaction force is subtracted from this force. It is demonstrated (28) that the operator feels no modification of his/her own impedance, while both the perceived inertia and damping of the haptic interface are decreased by $1 + K_f$.

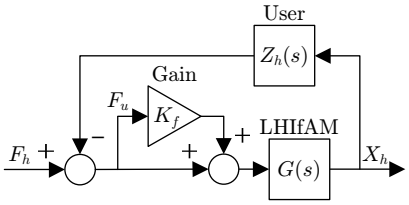

Fig. 20. Continuous model of the system in free movement.

The higher the gain K_f, the lower interface impedance is felt.

$$\frac{X_h(s)}{F_h(s)} = \frac{1}{\frac{m}{1+K_f}s^2 + \frac{b}{1+K_f}s + Z_h(s)} \tag{28}$$

A number of experiments have been performed demonstrating how this strategy significantly decreases the inertia felt. User's force F_h and position X_h have been measured in free movement with the motors turned off, and setting K_f equal to 2. Since inertia relates force with acceleration, abrupt forces and sudden accelerations have been exerted at several frequencies to obtain useful information in the Bode diagrams. The diagrams in Fig. 21 were obtained by using Matlab command *tfe* to the measured forces and displacements. This command computes the transfer function by averaging estimations for several time windows.

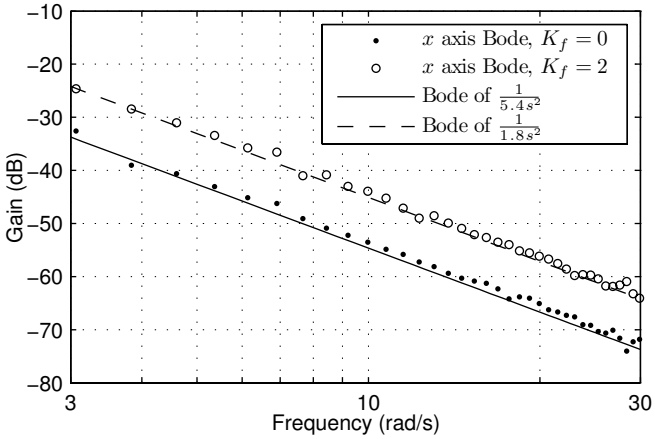

Fig. 21. Experimental gain Bode diagram of $\frac{X_h(s)}{F_h(s)}$ with $K_f = 0$ (dots) and $K_f = 2$ (circles); and theoretical gain Bode diagram of a mass of 5.4 kg (solid) and 1.8 kg (dashed).

As it could be expected, the gain Bode diagram of $\frac{X_h(s)}{F_h(s)}$ increases approximately 9.54 dB and the inertia felt is three times smaller. It can be also seen that, although it is not noticeable by the user, the force sensor introduces noise in the system. Its effect and other factors compromising the stability of the system will be studied in the following sections. The reader can found further details in (Gil, Rubio & Savall, 2009).

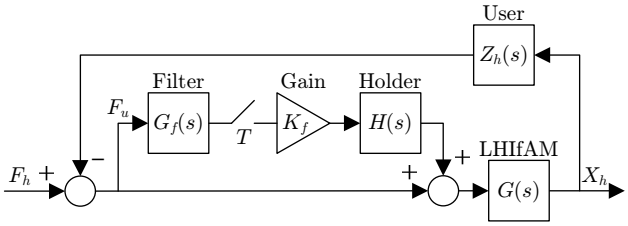

Fig. 22. Sampled model of the system in free movement.

5.1 Discrete Time Model

The sampling process limits the stability of the force gain K_f. A more rigorous model of the system, Fig. 22, is used to analyse stability and pinpoint the maximum allowable value of the force gain—and hence the maximum perceived decrease in inertia. This model introduces the sampling of the force signal, with a sampling period T, a previous anti-aliasing filter $G_f(s)$, and a zero-order holder $H(s)$. The characteristic equation of this model is

$$1 + K_f Z\left[H(s)\frac{G(s)Z_h(s)}{1+G(s)Z_h(s)}G_f(s)\right] = 1 + K_f G_1(z) = 0. \tag{29}$$

To obtain reasonable values for K_f, a realistic human model is needed. The one proposed by (Yokokohji & Yoshikawa, 1994) will be used in this case, because in this model the operator grasps the device in a similar manner. The dynamics of the operator (30) is represented as a spring-damper-mass system where m_h, b_h and k_h denote mass, viscous and stiffness coefficients of the operator respectively. Regarding the filter, the force sensor used in the LHIfAM (SI-40-2 Mini40, ATI Industrial Automation), incorporates a first order low-pass filter at 200 Hz (31). The control board of the system (dSPACE DS1104) runs at 1 kHz.

$$Z_h(s) = m_h s^2 + b_h s + k_h = 2s^2 + 2s + 10 \tag{30}$$

$$G_f(s) = \frac{1}{1+T_f s} = \frac{1}{1+0.005s} \tag{31}$$

Using these expressions, the critical force gain for the LHIfAM is

$$K_{fCR} = \mathrm{Gm}\{G_1(z)\} = 37.12. \tag{32}$$

This means that the inertia could be theoretically reduced from 5.4 kg up to 0.14 kg. However, phase crossover frequency coincides with the Nyquist frequency (see Fig. 23). At this frequency, as shown in previous section, vibration modes of the interface—which were not modelled in $G(s)$—play an important role in stability.

Possible time delays in the feedforward loop will reduce the critical force gain value because phase crossover will take place at a lower frequency. In case of relatively large delays, the worst value of the critical force gain is approximately

$$K_{fCR}^{W} = 1 + \frac{m}{m_h}, \tag{33}$$

where "W" denotes "worst case". This worst value has been defined within the wide range of frequencies in which the influence of inertia is dominant and the gain diagram is nearly constant (see Fig. 23). According to (33), several statements hold true:

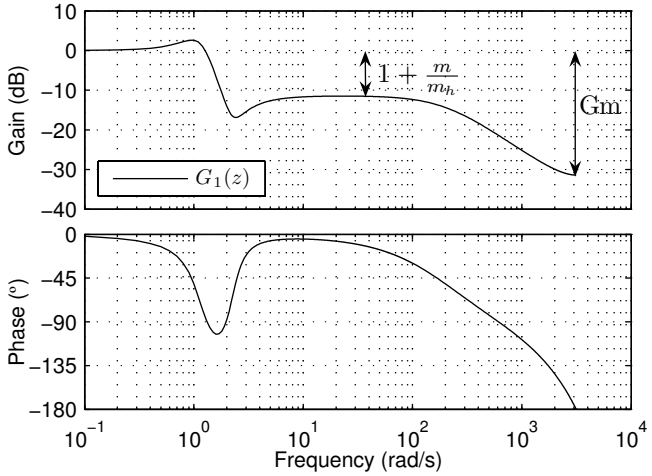

Fig. 23. Bode diagram of $G_1(z)$ using the estimated transfer function of the LHIfAM, the antialiasing filter (31) and the human model proposed by (Yokokohji & Yoshikawa, 1994). The gain is $1+\frac{m}{m_h}$ (in dB) for a wide range of frequencies.

- The larger the human mass m_h which is involved in the system, the lower the critical force gain K_{fCR} will be. This equivalent human mass will be similar to the mass of the finger, the hand or the arm, depending on how the operator grasps the interface.
- Even in the worst-case scenario—assigning an infinite mass to the operator or a very low mass to the device—the force gain K_f can be set to one, and hence, the inertia can be halved.

The first statement is consistent with a common empirical observation, (Carignan & Cleary, 2000), (Gillespie & Cutkosky, 1996): the haptic system can be either stable or unstable, depending on how the user grasps the interface.

5.2 Inclusion of Digital Filtering

According to (Carignan & Cleary, 2000) and (Eppinger & Seering, 1987), since the force sensor of the LHIfAM is placed at the end-effector, the unmodelled modes of the mechanism introduce appreciable high-frequency noise in its measurements. Therefore, the inclusion of a digital filter in the force feedforward loop is required. Fig. 24 shows the block diagram with the digital filter, whose transfer function is $D(z)$.
The new theoretical critical force gain of the system,

$$K_{fCR} = \mathrm{Gm}\{D(z)G_1(z)\}, \tag{34}$$

can be higher than (33). However, the phase crossover frequency will be placed at a higher frequency, where unmodelled dynamics introduces new poles and zeros that may drive the system into instability. Therefore, a more complete model of the system $G(s)$ including these vibration modes should be used in (34).
Nevertheless, it is not necessary to find a complex model of the system to tune the cut-off frequency of the digital filter. There are two boundaries for this frequency: a lower boundary

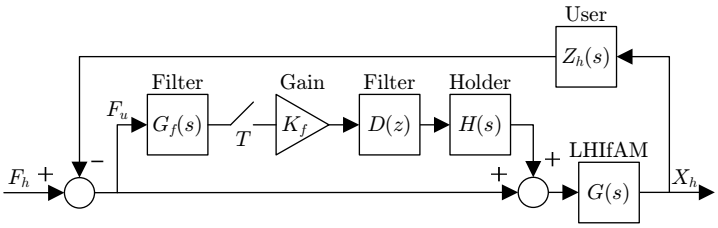

Fig. 24. Final force feedforward strategy with digital filter.

imposed by the bandwidth of human force and an upper one derived by the first vibration mode of the mechanism. Regarding the lower boundary, since the power spectrum of the human hand achieves about 10 Hz (Lawrence et al., 1996), the cut-off frequency should be above this value. Otherwise, the operator feels that the system is unable to track her/his "force commands". On the other hand, the first vibration mode of the interface mechanism should be considered as the upper boundary. Previous section has shown that a significant resonant peak appears around 82 Hz in the LHIfAM (Fig. 15). These facts motivate the inclusion of a second-order Butterworth digital filter at 30 Hz for this interface. And the final force gain K_f implemented in the system is equal to 5. With this value the apparent inertia of the device in the x direction is 0.9 kg, which matches the inertia in the other translational directions so the inertia tensor becomes almost spherical for this gain. In Fig. 25, the frequency response along the controlled x axis is compared with the y axis.

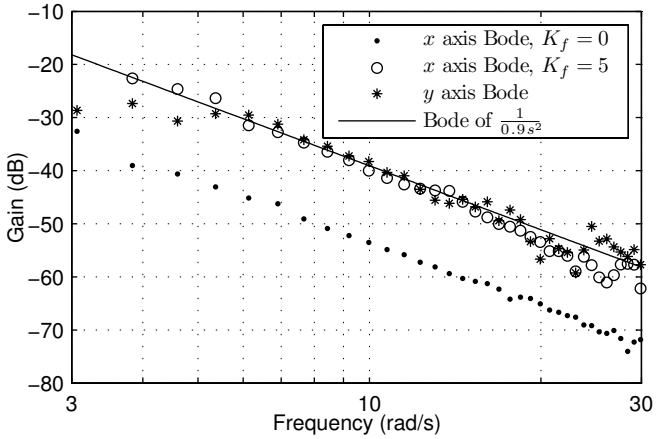

Fig. 25. Experimental gain Bode diagrams of the LHIfAM along y axis (stars), and along x axis with $K_f = 0$ (dots) and $K_f = 5$ (circles).

6. Conclusion and Future Directions

This chapter has started by analysing the influence of viscous damping and delay on the stability of haptic systems. Although analytical expressions of the stability boundaries are quite

complex, a linear condition relating stiffness, damping and time delay has been proposed and validated with experiments.
Since the analyses presented in this chapter assume the linearity of the system, its results can only be taken as an approximation if non-linear phenomena (e.g. Coulomb friction and sensor resolution) are not negligible. Another limit is the required low bandwidth of the system compared to the sampling rate, which may be violated, e.g. if the haptic device collides with a real environment.
Beyond the rigid haptic model, the influence of internal vibration modes on the stability has also been studied. Haptic models commonly used to analyse stability rarely take into account this phenomenon. This work shows that the resonant mode of cable transmissions used in haptic interfaces can affect the stability boundary for haptic rendering. A criterion that estimates when this fact occurs is presented, and experiments have been carried out to support the theoretical conclusions.
Finally, a force feedforward scheme has been proposed to decrease the perceived inertia of a haptic device, thereby improving system transparency. The force feedforward strategy has been successfully applied to the LHIfAM haptic device, showing its direct applicability to a real device and its effectiveness in making LHIfAM's inertia tensor almost spherical.
In terms of future research, the investigation of nonlinear effects on stability is necessary to be carried out. Also the robustness against uncertainties of physical parameters and external disturbances has to be examined.
The authors hope that the research included in this chapter will provide a better understanding of the many phenomena that challenge the development of haptic controllers able to display a wide dynamic range of impedances while preserving stability and transparency, and thereby improve the performance of present and future designs.

7. References

Abbott, J. J. & Okamura, A. M. (2005). Effects of position quantization and sampling rate on virtual-wall passivity, *IEEE Trans. Robot.* **21**(5): 952–964.

Adams, R. J. & Hannaford, B. (1999). Stable haptic interaction with virtual environments, *IEEE Trans. Robotic. Autom.* **15**(3): 465–474.

Barbé, L., Bayle, B. & de Mathelin, M. (2006). Towards the autotuning of force-feedback teleoperators, *8th Int. IFAC Symposium on Robot Control*, Bologna, Italy.

Basdogan, C., De, S., Kim, J., Muniyandi, M., Kim, H. & Srinivasan, M. A. (2004). Haptics in minimally invasive surgical simulation and training, *IEEE Comput. Graph. Appl.* **24**(2): 56–64.

Bernstein, N. L., Lawrence, D. A. & Pao, L. Y. (2005). Friction modeling and compensation for haptic interfaces, *WorldHaptics Conf.*, Pisa, Italy, pp. 290–295.

Bonneton, B. & Hayward, V. (1994). Implementation of a virtual wall, *Technical report*, McGill University.

Borro, D., Savall, J., Amundarain, A., Gil, J. J., García-Alonso, A. & Matey, L. (2004). A large haptic device for aircraft engine maintainability, *IEEE Comput. Graph. Appl.* **24**(6): 70–74.

Brown, J. M. & Colgate, J. E. (1994). Physics-based approach to haptic display, *ISMRC Topical Workshop on Virtual Reality*, Los Alamitos, CA, USA, pp. 101–106.

Carignan, C. R. & Cleary, K. R. (2000). Closed-loop force control for haptic simulation of virtual environments, *Haptics-e* **1**(2).

Çavuşoğlu, M. C., Feygin, D. & Frank, T. (2002). A critical study of the mechanical and electrical properties of the phantom haptic interface and improvements for high-performance control, *Presence: Teleoperators and Virtual Environments* **11**(6): 555–568.

Colgate, J. E. & Brown, J. M. (1994). Factors affecting the z-width of a haptic display, *IEEE Int. Conf. Robot. Autom.*, Vol. 4, San Diego, CA, USA, pp. 3205–3210.

Colgate, J. E. & Schenkel, G. (1997). Passivity of a class of sampled-data systems: Application to haptic interfaces, *J. Robot. Syst.* **14**(1): 37–47.

Díaz, I. n. & Gil, J. J. (2008). Influence of internal vibration modes on the stability of haptic rendering, *IEEE Int. Conf. Robot. Autom.*, Pasadena, CA, USA, pp. 2884–2889.

Diolaiti, N., Niemeyer, G., Barbagli, F. & Salisbury, J. K. (2006). Stability of haptic rendering: Discretization, quantization, time-delay and coulomb effects, *IEEE Trans. Robot.* **22**(2): 256–268.

Eppinger, S. D. & Seering, W. P. (1987). Understanding bandwidth limitations in robot force control, *IEEE Int. Conf. Robot. Autom.*, Vol. 2, Raleigh, NC, USA, pp. 904–909.

Frisoli, A., Sotgiu, E., Avizzano, C. A., Checcacci, D. & Bergamasco, M. (2004). Force-based impedance control of a haptic master system for teleoperation, *Sensor Review* **24**(1): 42–50.

Gil, J. J., Avello, A., Rubio, A. & Flórez, J. (2004). Stability analysis of a 1 dof haptic interface using the routh-hurwitz criterion, *IEEE Tran. Contr. Syst. Technol.* **12**(4): 583–588.

Gil, J. J., Rubio, A. & Savall, J. (2009). Decreasing the apparent inertia of an impedance haptic device by using force feedforward, *IEEE Tran. Contr. Syst. Technol.* **17**(4): 833–838.

Gil, J. J., Sánchez, E., Hulin, T., Preusche, C. & Hirzinger, G. (2009). Stability boundary for haptic rendering: Influence of damping and delay, *J. Comput. Inf. Sci. Eng.* **9**(1): 011005.

Gillespie, R. B. & Cutkosky, M. R. (1996). Stable user-specific haptic rendering of the virtual wall, *ASME Int. Mechanical Engineering Congress and Exposition*, Vol. 58, Atlanta, GA, USA, pp. 397–406.

Gosline, A. H., Campion, G. & Hayward, V. (2006). On the use of eddy current brakes as tunable, fast turn-on viscous dampers for haptic rendering, *Eurohaptics Conf.*, Paris, France.

Hannaford, B. & Ryu, J.-H. (2002). Time domain passivity control of haptic interfaces, *IEEE Trans. Robot. Autom.* **18**(1): 1–10.

Hashtrudi-Zaad, K. & Salcudean, S. E. (1999). On the use of local force feedback for transparent teleoperation, *IEEE Int. Conf. Robot. Autom.*, Detroit, MI, USA, pp. 1863–1869.

Hirzinger, G., Sporer, N., Albu-Schäffer, A., Hähnle, M., Krenn, R., Pascucci, A. & Schedl, M. (2002). DLR's torque-controlled light weight robot III - are we reaching the technological limits now?, *IEEE Int. Conf. Robot. Autom.*, Washington D.C., USA, pp. 1710–1716.

Hulin, T., Preusche, C. & Hirzinger, G. (2006). Stability boundary for haptic rendering: Influence of physical damping, *IEEE Int. Conf. Intell. Robot. Syst.*, Beijing, China, pp. 1570–1575.

Hulin, T., Preusche, C. & Hirzinger, G. (2008). Stability boundary for haptic rendering: Influence of human operator, *IEEE Int. Conf. Intell. Robot. Syst.*, Nice, France, pp. 3483–3488.

Hulin, T., Sagardia, M., Artigas, J., Schätzle, S., Kremer, P. & Preusche, C. (2008). Human-scale bimanual haptic interface, *Enactive Conf. 2008*, Pisa, Italy, pp. 28–33.

Janabi-Sharifi, F., Hayward, V. & Chen, C. (2000). Discrete-time adaptive windowing for velocity estimation, *IEEE Tran. Contr. Syst. Technol.*, Vol. 8, pp. 1003–1009.

Kuchenbecker, K. J. & Niemeyer, G. (2005). Modeling induced master motion in force-reflecting teleoperation, *IEEE Int. Conf. Robot. Autom.*, Barcelona, Spain, pp. 350–355.

Lawrence, D. A., Pao, L. Y., Salada, M. A. & Dougherty, A. M. (1996). Quantitative experimental analysis of transparency and stability in haptic interfaces, *ASME Int. Mechanical Engineering Congress and Exposition*, Vol. 58, Atlanta, GA, USA, pp. 441–449.

Ljung, L. (1999). *System Identification: Theory for the User*, Prentice Hall.

Mehling, J. S., Colgate, J. E. & Peshkin, M. A. (2005). Increasing the impedance range of a haptic display by adding electrical damping, *First WorldHaptics Conf.*, Pisa, Italy, pp. 257–262.

Minsky, M., Ouh-young, M., Steele, O., Brooks Jr., F. & Behensky, M. (1990). Feeling and seeing: Issues in force display, *Comput. Graph.* **24**(2): 235–243.

Åström, K. J. & Hägglund, T. (1995). *PID Controllers: Theory, Design, and Tuning*, Instrument Society of America, North Carolina.

Ryu, J.-H., Preusche, C., Hannaford, B. & Hirzinger, G. (2005). Time domain passivity control with reference energy following, *IEEE Tran. Contr. Syst. Technol.* **13**(5): 737–742.

Salcudean, S. E. & Vlaar, T. D. (1997). On the emulation of stiff walls and static friction with a magnetically levitated input/output device, *Journal of Dynamics, Measurement and Control* **119**: 127–132.

Savall, J., Borro, D., Amundarain, A., Martin, J., Gil, J. J. & Matey, L. (2004). LHIfAM - Large Haptic Interface for Aeronautics Maintainability, *IEEE Int. Conf. Robot. Autom.*, Video Proceedings, New Orleans, LA, USA.

Savall, J., Martín, J. & Avello, A. (2008). High performance linear cable transmission, *Journal of Mechanical Design* **130**(6).

Tognetti, L. J. & Book, W. J. (2006). Effects of increased device dissipation on haptic two-port network performance, *IEEE Int. Conf. Robot. Autom.*, Orlando, FL, USA, pp. 3304–3311.

Townsend, W. T. (1988). *The Effect of Transmission Design on Force-controlled Manipulator Performance*, Ph.d. thesis, MIT Artificial Intelligence Laboratory.

Ueberle, M. & Buss, M. (2002). Design, control, and evaluation of a new 6 dof haptic device, *IEEE Int. Conf. Intell. Robot. Syst.*, Lausanne, Switzerland, pp. 2949–2954.

Weir, D. W., Colgate, J. E. & Peshkin, M. A. (2008). Measuring and increasing z-width with active electrical damping, *Int. Symp. on Haptic Interfaces*, Reno, NV, USA, pp. 169–175.

Yokokohji, Y. & Yoshikawa, T. (1994). Bilateral control of master-slave manipulators for ideal kinesthetic coupling. formulation and experiment, *IEEE Trans. Robot. Autom.* **10**(5): 605–620.